Pre-impact mutual orbit of the DART target binary asteroid (65803) Didymos derived from observations of mutual events in 2003–2021

Preprint submitted to Elsevier Preprint *10 May 2022*

Proposed running head: Didymos mutual orbit modeling

Abstract

We modeled photometric observations of mutual events (eclipses and occultations) between the components of the binary near-Earth asteroid (65803) Didymos, the target of the Double Asteroid Redirection Test (DART) space mission, that were taken from 2003 to 2021 (Pravec et al. 2022, submitted). We derived parameters of the modified Keplerian mutual orbit (allowing for a quadratic drift in the mean anomaly, which is presumably caused by an interplay between the BYORP effect and mutual tides, or by differential Yarkovsky force) of the secondary, called Dimorphos, around the Didymos primary and estimated its diameter. The J2000 ecliptic longitude and latitude of the orbital pole are $320.6^\circ \pm 13.7^\circ$ and $-78.6^\circ \pm 1.8^\circ$, respectively, and the orbital period is 11.921624 ± 0.000018 h at epoch JD 2455873.0 (asterocentric UTC; all quoted uncertainties correspond to 3σ, except the density estimate below). We obtained the quadratic drift of the mean anomaly of 0.15 ± 0.14 deg/yr^2. The orbital eccentricity is ≤ 0.03. We determined the ecliptic longitude and latitude of the radius vector of Dimorphos with respect to Didymos at the nominal time of the DART impact to Dimorphos (JD 2459849.46875 geocentric UTC) to be $222.8^\circ \pm 7.0^\circ$ and $-1.6^\circ \pm 4.2^\circ$, respectively. We also estimated the bulk density of the system to be 2.44 ± 0.30 g cm^{-3} (1σ uncertainty).

Key words: Asteroids, satellites; Photometry; DART space mission; Hera space mission

---

1 Introduction

The near-Earth asteroid (65803) Didymos, originally designated 1996 GT, was discovered by the *Spacewatch* asteroid survey from Kitt Peak Observatory in Arizona on 1996 April 11. Its binary nature was revealed by Pravec et al. (2003). Pravec et al. (2006) and Scheirich and Pravec (2009) analyzed and modeled photometric data obtained during its close approach to Earth in 2003. They reported initial estimates of the binary system properties, including parameters of the mutual orbit of the two components. The system was also observed using radar from Arecibo and Goldstone in 2003. The radar observations were published and modeled together with the photometric data by Naidu et al. (2020) who obtained a shape model of the primary and determined or constrained several parameters of the binary asteroid system.

Didymos is classified as an S-type asteroid (Cheng et al., 2018) based on vis-IR spectra obtained by de León et al. (2010), also confirmed by Dunn et al. (2013).

The secondary of the Didymos binary system, recently named Dimorphos, has been selected as a target of the Double Asteroid Redirection Test (DART). It is NASA's first planetary defense test mission, with the goal of demonstrating the kinetic impactor mitigation technique on an asteroid. It was launched in November 2021, and it will arrive at the Didymos system on the September 26, 2022 at 23:15 UTC and impact into Dimorphos. The main benefit of targeting a binary asteroid system on a kinetic impactor mission is that it allows the main result of the test – the change in the mutual orbital period – to be measured from Earth via photometric observations, assuming that the binary system exhibits mutual events seen from Earth (Cheng et al., 2015). Rivkin et al. (2021) discuss the factors that led to the recognition that Didymos was the best candidate for a kinetic impactor test, and its selection as the DART target. The Didymos system will be investigated by ESA's Hera mission from the beginning of 2027 for about half a year, which will provide a thorough description of the post-impact state of the binary system (Michel et al., 2022).

An important part of the preparation of the DART mission has been an observational effort to precisely determine the orbit of the secondary around the primary. For that, Pravec et al. (2022) obtained photometric observations of the Didymos system taken with several large- or medium-sized groundbased telescopes from 2015 to 2021. In this paper, we present results from mutual orbit modeling using the complete photometry data for mutual events in the Didymos system from 2003 to 2021. An independent derivation of the mutual orbit based on an analysis of mutual event timings has been made by Naidu et al. (2022).

2 Mutual orbit model of Didymos system

2.1 Observational data

The data used in our analysis, obtained during five apparitions of Didymos from 2003 to 2021, were published in Pravec et al. (2006, 2022). We briefly summarize them in Table 1. Each row in the table represents one apparition, identified with the mid-UTC date of its first and last observing sessions (runs) rounded to the nearest tenth of a day in the first column. Subsequent columns give the number of observing runs (labeled as *No. of nights*, but we note that they were taken using several telescopes and so more than one run was sometimes taken on a single night) in the given apparition and a reference to where more information on the observations is available.

The data were analysed using the standard technique described in Pravec et al. (2006, 2022). Briefly, by fitting a two-period Fourier series to data points taken outside mutual (occultation or eclipse) events, the rotational lightcurves of the primary and the secondary, which are additive in flux units, are separated. Subtracting the rotational lightcurve of the primary from the data, a long-period (orbital) lightcurve component containing the mutual events and the secondary rotation lightcurve is obtained, which is then used for subsequent numerical modeling. We refer the reader to Pravec et al. (2022) for details of the lightcurve decomposition method.

Table 1
Photometric observations of the Didymos system

Time span	No. of nights	Reference
2003-11-20.9 to 2003-12-20.3	17	P06
2015-04-13.3 to 2015-04-14.4	2	P22
2017-02-23.3 to 2017-05-04.3	13	P22
2019-01-31.4 to 2019-03-11.1	5	P22
2020-12-12.6 to 2021-03-06.3	15	P22

References: P06 (Pravec et al., 2006), P22 (Pravec et al., 2022)

2.2 Numerical model

We constructed the model of the Didymos system using the technique of Scheirich and Pravec (2009) which was further developed by Scheirich et al. (2015, 2021). In the following, we outline the basic points of the method, but we refer the reader to the 2009, 2015, and 2021 papers for details of the technique.

The binary asteroid components were represented with spheres or oblate (for the primary) and prolate (for the secondary) ellipsoids (the ellipsoidal shapes were used to check the sensitivity of the solution to the shapes of the components, see below), orbiting each other on a circular orbit. We choose the circular orbit for simplicity, as the upper limit on the eccentricity is low (see below). The motion was assumed to be Keplerian, but we allowed for a quadratic drift in the mean anomaly. The spin axis of the primary was assumed to be normal to the mutual orbital plane of the components (i.e., we assumed zero inclination of the mutual orbit. See Appendix A for an assessment of this assumption.). When the secondary was modeled as the prolate spheroid, its long axis was kept aligned with the centers of the two bodies (i.e., in synchronous rotation with zero libration). The shapes were approximated with 1016 and 252 triangular facets for the primary and the secondary, respectively. The components were assumed to have the same albedo and to be exempt from albedo features (see Kaasalainen and Torppa, 2001, for discussion on why albedo features can be neglected). The brightness of the system as seen by the observer was computed as a sum of contributions from all visible facets using a ray-tracing code that checks which facets are occulted by or are in shadow from the other body. A combination of Lommel-Seeliger and Lambert scattering laws was used (see, e.g., Kaasalainen et al., 2002).

The quadratic drift in the mean anomaly, ΔM_d, was fitted as an independent parameter. It is the coefficient in the second term of the expansion of the time-variable mean anomaly:

$$M(t) = M(t_0) + n(t - t_0) + \Delta M_d (t - t_0)^2, \tag{1}$$

where

$$\Delta M_d = \frac{1}{2}\dot{n}, \tag{2}$$

where n is the mean motion, t is the time, and t_0 is the epoch. ΔM_d was stepped from -10 to $+10$ deg/yr^2 with a step of 0.01 deg/yr^2, and all other parameters were fitted at each step.

Since the 3-σ upper limit on the eccentricity of the mutual orbit is 0.03 only (Scheirich and Pravec, 2009), we set the eccentricity equal to zero for simplicity and efficiency. This assumption had a negligible effect on the accuracy of other derived parameters of the models. Scheirich and Pravec (2009) estimated the upper limit on the eccentricity using the data from the 2003 apparition. We checked that their upper limit is consistent with the data taken in 2015 to 2021, but those later data do not possess the characteristics necessary to use them for constraining the eccentricity more. Those characteristics include sufficient quality, time coverage, and depths of the mutual events. Thus, the constraint on the eccentricity by Scheirich and Pravec (2009) still applies.

Besides the data quality, constraining the eccentricity is also limited by presence of systematic modeling errors for the timings of mutual events. The model systematics are caused by the simplification of the shape of the primary (see below and Fig. 9), which can be up to 5 minutes for the Didymos system. Generally, mutual events between bodies on an eccentric orbit occur at times that are offset from the times of events for a circular orbit. For eccentricity of 0.03, these offsets are between 0 and 5 minutes (corresponding to between 0 and 2.5° in the mean anomaly of the secondary) for near-central events occurring close to the primary's equator and between 0 and 8 minutes (between 0 and 5° in mean anomaly) for non-central events occurring close to the primary's pole. **The systematic modeling errors can be confused with the event time offsets caused by non-zero eccentricity because they are comparable in magnitude.** To reduce the effect of the systematic modeling errors on eccentricity estimation, either a high number of mutual events would have to be observed so that we get a set of event timings taken at many different primary rotational phases that would average out the shape modeling errors, or use a detailed shape model for the primary (which may be constructed from resolved images that will be taken by DART).

Across all observations, we found a unique solution for the system parameters, see Table 2. We describe and discuss these parameters in Section 3.

We estimated uncertainties of the fitted parameters using two techniques. The uncertainties of the relative semimajor axis and the orbital pole (these parameters are strongly determined by the shapes of the mutual events) were estimated using the procedure described in Scheirich and Pravec (2009). The uncertainties of the rest of the parameters, which are determined primarily by the timings of the events, were estimated using the method described in Scheirich et al. (2021), which we outline below.

The residuals of the model fitted to the observational data do not obey the Gaussian statistics because of systematic errors resulting from model simplifications. In particular, the residuals of nearby measurements appear correlated. To eliminate the effect we adopted the following strategy based on the χ^2 test.

We choose a correlation time d and for each data point (i) we calculated how many other data points, K_i, are within $\pm d/2$ from the given point. We then applied a weight of $1/K_i$ to the given data point in the χ^2 sum. We also calculated an effective number of data points as $N_{\mathrm{eff}} = \sum_{i=1}^{N} 1/K_i$, where N is the total number of data points. For normalized χ^2 we then have $\chi^2 = 1/(N_{\mathrm{eff}} - M)\sum_{i=1}^{N}(O-C)_i^2/(\sigma_i^2 K_i)$, where M is the number of fitted parameters of the model and σ_i is a standard deviation of the ith point. As the residuals are predominated by model rather than observational uncertainties, we assign each data point the same standard deviation $\sigma_i = \sigma$, where σ is the RMS residual (root mean square of observed magnitudes, O, minus the values calculated from the model, C) of the best fit solution. An illustration of the weights $1/K_i$ determination is shown in Fig. 1. In Fig. 2, the distribution of residuals with and without the weights applied is shown for comparison.

The procedure described above is equivalent to reducing the number of data points to one in each time interval with the length d (i.e., to reducing the total number of points to N_{eff}) and assigning $(O-C)^2$ of this point to be a mean of $(O_i - C_i)^2$ of all the points within the interval. However, our approach has the advantage that it does not depend on a particular realization of dividing the observing time span into the intervals of length d.

We choose the correlation time d to be equal to 1/2 of the mean duration of a descending/ascending branch [1] of the secondary mutual event, i.e., the mean time between the first and the second or between the third and the fourth contact. For the observed events in Didymos, it is $d = 0.14$ h. (We also tested d to be twice as long, i.e., equal to the full mean duration of the secondary event branch, but we found it to be inadequate as the longer correlation time resulted in a substantial loss of information by deweighting the datapoints too much.)

We note that the mutual orbit model fit is sensitive only to data points covering mutual events and their closest neighborhood. Therefore we limited the above analysis only to such data points; points further outside the events were not used, because they do not effectively contribute to the determination of the mutual orbit.

Upon stepping a given parameter on a suitable interval (while the other parameters fitted) and computing the normalized χ^2 for each step, we determined 3-σ uncertainty of the given parameter as an interval in which χ^2 is below the p-value of the χ^2 test, corresponding to the probability that the χ^2 exceeds a particular value only by chance equal to 0.27%.

Plot of the normalized χ^2 vs ΔM_d is shown in Fig. 3. In order to save computing time, the plots were constructed using spherical shapes for both components. However, a neighborhood of the best solution was then revisited using ellipsoidal shapes in order to check the sensitivity of the solution to the shapes of the components. No significant change of the solution was found for the polar flattening of the primary up to 1.4 and the equatorial elongation of the secondary up to 1.5. We took these values as the upper limits from Naidu et al., 2020 (the 3σ upper limit for the flattening of the primary) and Pravec et al. 2016 (the upper limit for the elongation of the secondary based on statistics of other small binary asteroids), respectively.

The long-period (orbital) lightcurve component data together with the synthetic lightcurve of the best-fit solution are presented in Figs. 4 to 7. A close examination of the figures reveals that while most of the observed events are fitted well, there are some small or moderate discrepancies between the best-fit model and the data in several mutual events. Those include (a) inprecisely modeled shapes of some primary minima, (b) time offsets of some descending or ascending branches of the events or (c) incorrect depths/lengths of some partial events. We ascribe these discrepancies to the model simplifications, namely to the spherical or ellipsoidal approximation of the shape of the primary. Local topography features on the disc (for the case a) or on the limb (for the cases b and c) of the primary are suspected to be causes of the respective effects.

The uncertainty area of the orbital pole is shown in Fig. 8. Figure 9 shows the quadratic drift in the mean anomaly, ΔM, which was computed as follows. We generated a synthetic lightcurve using the model with parameters from the best-fit solution except ΔM_d, which was fixed at zero. Then, for each lightcurve event

---

[1] We define a *branch* as a part of the mutual event in the lightcurve, where the brightness of the system is rapidly decreasing or increasing, i.e., the time period during which the eclipsed/occulted body is immersing into or emerging from the shadow of, or is disappearing behind or reappearing from behind the other body.

separately, we fitted the mean anomaly of the model in order to obtain the best match between its synthetic lightcurve and the observed data. ΔM is a difference between the mean anomaly of the original model and the fitted one. For each event, we computed also a standard deviation of ΔM using the procedure described above, but with χ^2 computed only from the data points in the vicinity of the mutual event in question.

3 Parameters of Didymos system

In this section, we summarize the best-fit model parameters of the Didymos binary system that we obtained or took from previous publications. The parameters are listed in Table 2.

In the first part of the table, we present data derived from optical and spectroscopic observations of the system. H_V and G are the mean absolute magnitude and the phase parameter of the H–G phase relation (Bowell et al., 1989). $p_{\rm V}$ is the visual geometric albedo derived by Naidu et al. (2020) using H_V and the effective diameter of the whole system from the 3D radar model.

Didymos is classified as an S-type asteroid (Cheng et al., 2018) based on vis-IR spectra obtained by de León et al. (2010).

In the next two parts of Table 2, we give parameters for the components of the binary. The indices 1 and 2 refer to the primary and the secondary, respectively.

$D_{1,\rm C}$ and $D_{2,\rm C}$ are the mean (rotationally averaged) cross-section equivalent diameters (i.e., the diameter of a sphere with the same cross-section) of the primary and secondary, respectively, at the mean aspect of observed total secondary events (see below).

To quantify the mean aspect we used an asterocentric latitude of the Phase Angle Bisector (PAB), which is the mean direction between the heliocentric and geocentric directions to the asteroid. As discussed in Harris et al. (1984), this is an approximation for the effective viewing direction of an asteroid observed at the non-zero solar phase. The average absolute value of the asterocentric latitude of the PAB for the observed total events was 9.7°. (We computed the latitude of the PAB using the nominal pole of the mutual orbit and assuming that the spin poles of both components are the same as the orbit pole.)

$D_{1,\rm V}$ and $D_{2,\rm V}$ are the volume equivalent diameters (i.e., the diameter of a sphere with the same volume) of the primary and secondary, respectively. $D_{2,\rm C}/D_{1,\rm C}$ is the ratio between the mean cross-section equivalent diameters of the components. P_1 is the rotational period of the primary.

$(A_1B_1)^{1/2}/C_1$ is a ratio between the mean equatorial and the polar axes of the primary. A_1/B_1 is a ratio between the equatorial axes of the primary (equatorial elongation). ρ_1 is the bulk density of the primary.

Table 2

Parameters of Didymos system

Parameter		Value	Unc.	Reference
Whole system:				
Absolute magnitude	H_V	18.16 ± 0.04	1σ	P12
Phase parameter	G	0.20 ± 0.02	1σ	K04
Visual geom. albedo	p_{V}	0.15 ± 0.04	1σ	N20
Taxon. class		S		C18
Primary:				
Volume equiv. diameter	$D_{1,\mathrm{V}}$ (km)	0.780 ± 0.03	1σ	N20
Cross-section equiv. diameter	$D_{1,\mathrm{C}}$ (km)	0.786 ± 0.05	1σ	This work/N20[a]
Rotational period	P_1 (h)	2.2600 ± 0.0001	1σ	N20
Oblateness	$(A_1 B_1)^{1/2}/C_1$	$1.04^{+0.12}_{-0.04}$	1σ	N20[b]
Equatorial elongation	A_1/B_1	$1.02^{+0.09}_{-0.02}$	1σ	N20[b]
Bulk density	ρ_1 (g cm^{-3})	2.17 ± 0.35 / 2.44 ± 0.30	1σ	N20/This work
Secondary:				
Cross-section equiv. diam. ratio	$D_{2,\mathrm{C}}/D_{1,\mathrm{C}}$	0.217 ± 0.004[c]	1σ	This work
Cross-section equiv. diameter	$D_{2,\mathrm{C}}$ (km)	0.171 ± 0.011	1σ	This work
Volume equiv. diameter	$D_{2,\mathrm{V}}$ (km)	$\geq 0.171 \pm 0.011$	see text	This work
Mutual orbit:				
Sem. axis / primary diam.	$a/(A_1 B_1)^{1/2}$	$1.59 \pm 0.20/1.51 \pm 0.22$	3σ	This work/N20[d]
Semimajor axis	a (km)	1.19 ± 0.03	1σ	N20
Ecl. longitude of orbital pole	L_{P} (°)	320.6 ± 13.7[e]	3σ	This work
Ecl. latitude of orbital pole	B_{P} (°)	-78.6 ± 1.8	3σ	This work
Drift in mean anomaly	ΔM_d (deg/yr^2)	0.15 ± 0.14	3σ	This work
Mean motion rate	$\dot{n}$ (rad/s^2)	$5.26 \pm 4.91 \times 10^{-18}$	3σ	This work
Orbital period at t_0	P_{orb} (h)	11.921624 ± 0.000018	3σ	This work
Orbital period at t_{imp}	$P_{\mathrm{orb}}^{\mathrm{imp}}$ (h)	11.921473 ± 0.000138	3σ	This work
Mean anomaly at t_0	M_0 (°)	89.1[f]		This work
Eccentricity	e	≤ 0.03	3σ	SP09
Ecl. coordinates of the secondary wrt the primary at t_0				
	λ_0 (°)	320.7 ± 9.8[g]	3σ	This work
	β_0 (°)	11.5 ± 1.9	3σ	This work
Epoch	t_0	JD 2455873.0 (asterocentric UTC)		
Ecl. coordinates of the secondary wrt the primary at t_{imp}				
	λ_{imp} (°)	222.8 ± 7.0[g]	3σ	This work
	β_{imp} (°)	-1.6 ± 4.2	3σ	This work
Epoch of impact	t_{imp}	JD 2459849.46875 (geocentric UTC)		

References: C18: Cheng et al. 2018; K04: Kitazato et al. 2004; N20: Naidu et al. 2020; P12: Pravec et al. 2012; SP09: Scheirich and Pravec 2009.

[a] Derived using shape model from N20, see text for details. [b] Derived using DEEVE from N20, see text for details. [c] This is a ratio of the cross-section equivalent diameters for the average observed aspect of 9.7°. See text for details. [d] Derived using DEEVE from N20, see text for details. [e] For the actual shape of the uncertainty area, see Fig. 8. Semiaxes of the area are 1.8 × 3.0°. [f] We do not report the uncertainty of M_0, since it is strongly correlated with L_{P}. Instead, we report uncertainties of λ_0 and β_0. [g] For the actual shape of the uncertainty areas of λ_0 vs. β_0 and λ_{imp} vs. β_{imp}, see Fig. 10.

$D_{1,\mathrm{V}}$ and the rotational period of the primary were taken from Naidu et al. (2020). $D_{1,\mathrm{C}}$ was computed from a mean (rotationally averaged) cross-section of the radar shape model from Naidu et al. (2020) at the mean aspect of the observed total events (asterocentric latitude of the PAB being 9.7°). We adopted a 6% relative uncertainty for $D_{1,\mathrm{C}}$. We note that Naidu et al. (2020) give three uncertainties – 4% for the volume-equivalent diameter of the primary, 6% for the extents along x and y principal axes of the primary, and 10% for the extent along z-axis. The 6% uncertainty appears relevant for our derivation of $D_{1,\mathrm{C}}$.

We derived $D_{2,\mathrm{C}}/D_{1,\mathrm{C}}$ from the depths of the observed total secondary events. For that, we used the high-quality data for the secondary events observed in November-December 2003, March 2019 and December 2020 (Pravec et al., 2022). The mean depth of the total secondary events was measured to be 0.050 ± 0.002 mag, which gives $D_{2,\mathrm{C}}/D_{1,\mathrm{C}} = 0.217 \pm 0.004$ (1-σ uncertainties).

From $D_{2,\mathrm{C}}/D_{1,\mathrm{C}}$ and $D_{1,\mathrm{C}}$ we computed $D_{2,\mathrm{C}}$. We note that Naidu et al. (2020) reported visible extents of the secondary in the radar data of 150 ± 30 m, which is consistent with our value.

To calculate the secondary volume equivalent diameter $D_{2,\mathrm{V}}$ from the determined $D_{2,\mathrm{C}}$, we need to use a shape model for the secondary. As Dimorphos' shape has not been determined yet, we explore a range of possible ellipsoidal shapes for it. For a spherical secondary, we have $D_{2,\mathrm{V}} = D_{2,\mathrm{C}}$. In a case the secondary is a prolate ellipsoid with $A_2/B_2 = 1.5$ and $B_2/C_2 = 1$ —we note that Pravec et al. (2016) found that the equatorial axis ratios of NEA and small MBA binaries show an upper limit of A_2/B_2 about 1.5, hence our choice of the extremally elongated ellipsoid here—, we obtain $D_{2,\mathrm{V}} = 0.173 \pm 0.011$ km. While we see here that the secondary volume equivalent diameter is relatively insensitive to the equatorial axis ratio A_2/B_2, it is more sensitive to B_2/C_2. Unfortunately there is no formal observational or theoretical constraint on the B_2/C_2 for Dimorphos. To show the sensitivity of $D_{2,\mathrm{V}}$ on the polar flattening of the secondary, we calculate $D_{2,\mathrm{V}}$ for an arbitrarily chosen value for B_2/C_2 of 1.5. For a case of the oblate secondary with $A_2/B_2 = 1$ and $B_2/C_2 = 1.5$ we obtain $D_{2,\mathrm{V}} = 0.181 \pm 0.012$ km, while for a case of $A_2/B_2 = 1.5$ and $B_2/C_2 = 1.5$ we obtain $D_{2,\mathrm{V}} = 0.183 \pm 0.012$ km.

Other quantities reported above were taken or derived using data from other sources as we describe in the following.

The mutual orbit and shapes of the Didymos components were modeled by Naidu et al. (2020) from radar observations taken in 2003. They reported the size of the primary to be close to a triaxial ellipsoid with axes 797 × 783 × 761 m (1σ uncertainties of ± 6%, 6% and 10%, respectively). The dimensions given are extents of a dynamically equivalent equal-volume ellipsoid (DEEVE; a homogeneous ellipsoid having the same moments of inertia and volume as the shape model). We used these values to derive $(A_1B_1)^{1/2}/C_1$ and A_1/B_1.

The bulk density of the primary (which they assume is the same as the bulk density of the whole system) was taken from Naidu et al. (2020). For comparison, we derived the bulk density of the whole system from the mutual orbital elements obtained in our work, which leads to 2.44 ± 0.30 g cm^{-3} (1σ). The derivation of the bulk density is as follows.

Assuming that both components have same bulk density, Kepler's third law can be written in the form (see Scheirich and Pravec, 2009)

$$\frac{4\pi^2}{G{P_{\mathrm{orb}}}^2}\left[\frac{V_2}{V_1}+1\right]^{-1}\frac{a^3}{V_1}=\rho, \tag{3}$$

where ρ is the bulk density, G is the gravitational constant, V_2 and V_1 are volumes of the secondary and the primary, respectively, a is the semimajor axis and P_{orb} is the orbital period. If the primary shape is assumed to be homogenous oblate ellipsoid and considering the effect of the oblateness up to the J_2 term (the first zonal harmonic coefficient in the gravitational potential expansion), the form can be modified to (see Rossi et al., 1999):

$$\frac{4\pi^2 a^3}{G{\mathbf{P}_{\mathrm{orb}}}^2(V_1+V_2)}\,\epsilon=\rho, \tag{4}$$

where

$$\epsilon = 1-\frac{3}{10}\frac{A_1^2-C_1^2}{a^2}, \tag{5}$$

where A_1 and C_1 are equatorial and polar axes of the primary, respectively.

We estimated the bulk density (presented in Table 2) using the spherical approximation for shapes of both components, which fit the photometry data best. The equation we used is

$$\rho=\frac{24\pi}{G{P_{orb}}^2}\left[\left(\frac{D_{2,\mathrm{V}}}{D_{1,\mathrm{V}}}\right)^3+1\right]^{-1}\left(\frac{a}{D_{1,\mathrm{V}}}\right)^3. \tag{6}$$

(We note that for spherical shapes $D_{1,\mathrm{V}} = D_{1,\mathrm{C}} = (A_1B_1)^{1/2}$ and $D_{2,\mathrm{V}} = D_{2,\mathrm{C}}$.)

The relative semimajor axis value given in Table 2 was also derived using the assumption of spherical primary. To test the effect of flattening of the primary on the derivation of a and ρ, we also fitted the data with $(A_1B_1)^{1/2}/C_1$ fixed on three other values: 1.04, 1.16 and 1.40 (these were the nominal value, its 1σ upper limit and 3σ upper limit, respectively, taken from Naidu et al., 2020.). The results which we obtained for these values are given in Table 3.

To compare our Didymos' bulk density estimate with densities of other asteroids with similar composition, we computed a weighted mean of published estimated of mid- and small-sized S and Q-type asteroids, and

got a value of 2.31 g cm^{-3} (we did not include the bulk density of 3749 Balam to the weighted mean computation, since the value reported by Marchis et al., 2008, is only approximate and they did not estimate its uncertainty), see Table 4.

Table 3
The mutual semimajor axis and the bulk density of the Didymos system derived for different values of the flattening of the primary.

$(A_1B_1)^{1/2}/C_1$	$a/(A_1B_1)^{1/2}$ 3σ unc.	**Density** (g cm^{-3}), 1σ unc.
1.00	$\mathbf{1.59 \pm 0.20}$	$\mathbf{2.44 \pm 0.30}$
1.04	$\mathbf{1.56 \pm 0.20}$	$\mathbf{2.38 \pm 0.30}$
1.16	$\mathbf{1.48 \pm 0.19}$	$\mathbf{2.26 \pm 0.28}$
1.40	$\mathbf{1.33 \pm 0.13}$	$\mathbf{1.95 \pm 0.18}$

Table 4
Published estimates of the bulk density of mid- and small-sized S and Q-type asteroids

Name or designation	**Tax. class**	**Density** (g cm^{-3}), 1σ unc.	**Reference**
(243) Ida	**S**	2.6 ± 0.5	**Belton et al. (1995)**
(433) Eros	**S**	2.67 ± 0.03	**Yeomans et al. (2000)**
(5381) Sekhmet	**S**	1.98 ± 0.65	**Neish et al. (2003)**
(25143) Itokawa – ”head”	**S**	2.45 ± 0.23	**Kanamaru et al. (2019)**
(25143) Itokawa – ”body”	**S**	1.93 ± 0.05	**Kanamaru et al. (2019)**
(35107) 1991 VH	**Sq**	1.5 ± 0.17	**Pravec et al. (2006)**
(66063) 1998 RO1 – from 2003 data	**S**	$1.5^{+0.57}_{-0.20}$	**Scheirich and Pravec (200**
(66063) 1998 RO1 – from 2004 data	**S**	$4.1^{+0.27}_{-0.93}$	**Scheirich and Pravec (200**
(66391) Moshup – primary	**Q**	1.97 ± 0.24	**Ostro et al. (2006)**
(3749) Balam	**S**	~ 2.6	**Marchis et al. (2008)**

Carry (2012) made a statistical analysis of published estimates of the bulk densities of S-type asteroids and got an average value of 2.72 ± 0.54 **g cm^{-3} from the estimates more accurate than 20%. His value, however, is influenced by densities of large asteroids, which he also includes in his statistics.**

We note that our estimate of the bulk density of the Didymos system is consistent with that by Naidu et al. (2020) within the uncertainty intervals. It is possible that the value of the bulk density of 2.17 ± 0.35 **g cm^{-3} estimated by Naidu et al. (2020) is slightly underestimated while our value is slightly overestimated.**

In the last part of Table 2, we summarize the parameters of the mutual orbit of the binary components. $L_{\mathrm{P}}, B_{\mathrm{P}}$ are the ecliptic coordinates of the orbital pole in the equinox J2000, and M_0 is the mean anomaly of the secondary, measured from the ascending node (as pericenter is not defined for circular orbit) for epoch $t_0 =$

2455873.0 (asterocentric UTC, i.e., light-time corrected). Since M_0 is strongly correlated with L_P, we report only its value for the nominal solution and do not report its uncertainty (which is on the same order as the uncertainty of L_P). Instead, to describe the uncertainty of the position of the secondary in its orbit as an independent parameter, we report its relative ecliptic coordinates with respect to the primary (see below).

e is the orbit eccentricity (only its upper limit is given, reported by Scheirich and Pravec 2009), and ΔM_d is the quadratic drift in the mean anomaly. Since the orbital period P_orb changes with time, the value presented in Table 2 is for the epoch t_0. For this epoch, which is approximately the mean time of all observed events, a correlation between P_orb and ΔM_d is zero. We also give the time derivative of the mean motion $\dot{n}$, derived from ΔM_d, and the value of the orbital period at the nominal time of the DART impact $P_\mathrm{orb}^\mathrm{imp}$. **All periods presented in Table 2, i.e., P_1, P_orb and $P_\mathrm{orb}^\mathrm{imp}$, are sidereal.**

The uncertainty area of the orbit pole is shown in Fig. 8.

Naidu et al. (2020) give the value of the mutual semimajor axis to be 1.19 ± 0.03 km (1σ). To compare their result with our value, we computed $a/(A_1B_1)^{1/2}$ using their DEEVE for the primary and their semimajor axis of the mutual orbit. The result is given in Table 2.

λ_0 and β_0 are relative ecliptic coordinates of the secondary with respect to the primary at the epoch t_0. For the nominal time of the DART impact (t_imp = 2022-09-26.96875 geocentric UTC), these coordinates are given by λ_imp and β_imp.

Note that the uncertainty of λ_imp is smaller than the uncertainty of λ_0. This is because of the following: The time evolution of the uncertainty of λ is governed primarily by two factors: a) at the epochs covered with the data, it is restricted by their amount and quality; b) it grows quadratically into the future from the last observed apparition. Therefore, the uncertainty is small at the first and the last apparition (panels **a** and **c** on Fig. 10), while at t_0, which is not covered by the data, the uncertianty is larger (panel **b** on Fig. 10). The last panel (**d**) of Fig. 10 shows the uncertainty at the nominal time of the DART impact. To demonstrate the change of the uncertainty more illustratively, we constructed Fig. 11 showing an evolution of the 3-σ uncertainty of λ in time.

Although assuming that the Dimorphos orbit is coplanar with the primary's equator throughout the modeling presented above, we also examined the possibility that this assumption is not held. We obtained that the inclination of the Dimorphos orbit to the primary's equator is $\lesssim 3°$ (see Appendix A).

3.1 The inward drift of the mutual orbit

The mean anomaly of a changing orbit expanded to the second degree in time is expressed by Equations (1) and (2). ΔM_d can be expressed using the semimajor axis of the mutual orbit and its time derivative as

$$\Delta M_d = \frac{1}{2}\dot{n} = -\frac{3n\dot{a}}{4a}. \tag{7}$$

The observed value of $\Delta M_d = 0.15 \pm 0.14$ deg/yr^2 therefore imply an inward semi-major axis drift at the rate of $\dot{a} = -0.09 \pm 0.08$ cm/yr (3σ uncertainty).

Didymos system is the fourth binary for which we now have a long-term dynamical evolution inferred. The other three are (175706) 1996 FG3 that has a mean anomaly drift consistent with zero ($\Delta M_d = 0.04 \pm 0.20$ deg/yr^2, Scheirich et al., 2015), (66391) Moshup that shows an outward drift of the mutual orbit ($\Delta M_d = -0.65 \pm 0.16$ deg/yr^2, Scheirich et al., 2021), and (88710) 2001 SL9 that shows an inward drift of the mutual orbit (two solutions for ΔM_d: 2.8 ± 0.2 or 5.2 ± 0.2 deg/yr^2, Scheirich et al., 2021).

In the following, we discuss two possible mechanisms that can explain the slow inward drift of the Didymos system.

a) BYORP and tides

The binary YORP (BYORP) effect is a secular change of the mutual orbit of a binary asteroid system with a synchronous satellite due to the emission of thermal radiation from the asymmetric shape of that satellite. It was first hypothesized by Ćuk and Burns (2005). McMahon and Scheeres (2010a,b) built a detailed theory of the secular evolution of the mutual orbit due to the BYORP effect, which predicts that it causes the orbit to expand or contract on a timescale of thousands of years, as long as the satellite remains synchronous.

Adapting the method derived by McMahon and Scheeres (2010b), Pravec and Scheirich (2010) predicted[2] the quadratic drift of (65803) Didymos caused by BYORP to be 2.51 deg/yr^2. Our detected value, 0.15 ± 0.14 deg/yr^2 is much lower than this estimate. More recently, Jacobson and Scheeres (2011) presented an improved theory that incorporates both the BYORP effect and mutual tides between the two components. They showed that a stable long-term equilibrium may exist between these two torques if the BYORP effect is removing angular momentum from the orbit. Since the rotation period of Didymos is shorter than the orbital period of Dimorphos, the satellite raises a tidal bulge on the primary that removes energy from the rotation of the primary and transfers angular momentum to the mutual orbit. These two torques are opposite in sign and can balance one another because they depend differently on the mutual orbit semi-major axis. They evolve the mutual orbit to an equilibrium semi-major axis, where the mutual orbit no longer evolves (Scheirich et al., 2015, reported the first binary system observed to be in or very close to this equilibrium state).

The observed low positive value of the mean anomaly drift of Didymos may indicate that the system is evolving into and it is very close to, however not yet exactly at,

---

[2] This value of ΔM_d is based on a shape model of a secondary of another NEA binary – (66391) Moshup – and it is only a magnitude, not directional estimate.

such equilibrium.

b) Differential Yarkovsky force in binary asteroid system

Another effect causing a drift of the mutual semimajor axis is the Yarkovsky force, which affects not only the motion of the center of mass of the whole binary system but also the relative motion of components (Vokrouhlický et al., 2005). For NEA binaries, the semimajor axis drift is on the order from $\sim$0.1 mm/yr to several mm/yr (Scheirich et al., 2021), i.e., on the same order as the drift observed in the Didymos system. Besides the BYORP, the differential Yarkovsky force is therefore another possible mechanism explaining the drift.

4 Mutual events prediction for the 2022–2023 apparition

In order to facilitate planning ground-based observations before and after the DART impact, we computed times of mutual events that will occur in the 2022–2023 apparition using the nominal solution presented in Section 3. It is available at `https://asu.cas.cz/~asteroid/Didymos_2022-2023_events.htm`.

The list also includes the events for a period after the DART impact. Since the prediction in this period is made using the assumption that none of the orbital parameters will change, it has an informative character only.

5 Conclusions

The near-Earth asteroid (65803) Didymos is among the best characterized small asteroid binary systems. It is a typical member of the population of near-Earth asteroid binaries for most of its parameters. With the photometric data taken during five apparitions over the time interval of 17 years, we constrained its binary orbit and determined the relative position of its secondary (Dimorphos) at the time of the DART impact to within ±7.0° (3σ uncertainty) with respect to the primary.

We found that the mean motion of Dimorphos is increasing with a rate of $\dot{n} = 5.26 \pm 4.91 \times 10^{-18}$ rad/s^2 (3σ uncertainty), implying that the mutual semimajor axis is shrinking in time. After the near-Earth binary asteroid (88710) 2001 SL9 (Scheirich et al., 2021), this is the second case with this observed property. As the inward drift of its orbit can not be explained by mutual tides for the system with the rotation period of the primary shorter than the orbital period of the secondary (assuming the same sense of primary rotation and the mutual orbital motion), it suggests that either an interplay between the binary YORP (BYORP) effect and mutual tides, or the differential Yarkovsky force, or a combination of these effects, acts in the Didymos system.

Appendix A. Assessment of the mutual orbit nodal precession

In Section 2.2, the spin axis of the primary was assumed to be normal to the mutual orbital plane of the components. Here we examine if this assumption is reasonable and how the primary spin axis orientation affects the results.

In the case of spherical primary, the orientation of its spin axis has no effect either on the model lightcurve nor the results. In the case of an oblate primary, the main issue is that the orbital pole precedes around the spin pole of the primary when the two poles are not same. The nodal precession rate depends on the oblateness of the primary and other system parameters (see, e.g., Rossi et al., 1999). We tested three values of the primary oblateness: 1.04, 1.16 and 1.40 (i.e. the nominal value from Naidu et al. 2020 and its 1σ and 3σ upper limits, respectively). For these three values, the nodal precession rates are −1.61, −5.50 and −10.57°/day, respectively (we neglect the dependence of the nodal rate on the inclination of the satellite's orbit to the primary's equator because it is negligible for small angles).

We tested twelve orientations of the spin axis with respect to the orbital axis: four different orientations with an inclination between the axes of 1°, four with the inclination of 2°, and four with 4°. (The four orientations of the spin axis correspond to four different values of the length of ascending node of the satellite's orbit with respect to the primary's equator at the reference epoch.) For each combination of the orientation of the spin axis and the oblateness of the primary (the corresponding nodal rate was used for each oblateness), we then re-run the analysis.

From the best-fit solutions with inclinations of 1°, the largest absolute differences in parameters with respect to the nominal solution were: the difference in the mutual semimajor axis $\delta a/(A_1 B_1)^{1/2} = 0.07$, the difference in the orbital period $\delta P_{\mathrm{orb}} =$

0.00000072 h, the difference in the mean anomaly drift rate $\delta\Delta M_d = 0.016$ deg/yr^2, the differences in the relative ecliptic coordinates of the secondary with respect to the primary at the nominal time of the DART impact $\delta\lambda_{\mathrm{imp}} = 1.2°$, $\delta\beta_{\mathrm{imp}} = 0.7°$.

From the best-fit solutions with inclinations of 2°, the largest absolute differences in parameters with respect to the nominal solution were: $\delta a/(A_1B_1)^{1/2} = 0.11$, $\delta P_{\mathrm{orb}} = 0.00000096$ h, $\delta\Delta M_d = 0.016$ deg/yr^2, $\delta\lambda_{\mathrm{imp}} = 1.0°$, $\delta\beta_{\mathrm{imp}} = 1.5°$.

The best-fit solutions with inclinations of 4° are all inconsistent with the observed data. We obtain that the inclination of the Dimorphos orbit to the primary's equator is $\lesssim 3°$.

References

Belton, M. J. S., Chapman, C. R., Thomas, P. C., Davies, M. E., Greenberg, R., Klaasen, K., and 11 others, 1995. Bulk density of asteroid 243 Ida from the orbit of its satellite Dactyl. Nature, 374, 785-788.

Bowell, E., Hapke, B., Domingue, D., Lumme, K., Peltoniemi, J., Harris, A.W., 1989. Application of photometric models to asteroids. In: Asteroids II. Univ. Arizona Press, pp. 524-556.

Carry B., 2012. Density of asteroids. Planet. Space Sci., 73, 98118.

Cheng, A.F., et al., 2015. Asteroid impact and deflection assessment mission. Acta Astronaut. 115, 262–269.

Cheng, A.F., Rivkin, A.S., Michel, P., Atchison, J., Barnouin, O., Benner, L., Chabot, N.L., Ernst, C., Fahnestock, E.G., Kueppers, M., Pravec, P., Rainey, E., Richardson, D.C., Stickle, A.M., Thomas, C., 2018. AIDA DART asteroid deflection test: planetary defense and science objectives. Planet. Space Sci. 157, 104115.

de León, J., Licandro, J., Serra-Ricart, M., Pinilla-Alonso, N., Campins, H., 2010. Observations compositional, and physical characterization of near-Earth and Marscrosser asteroids from a spectroscopic survey. A&A 517, A23. https://doi.org/10.1051/0004-6361/200913852.

Dunn, T.L., Burbine, T.H., Bottke, W.F., Jr, Clark, J.P. 2013. Mineralogies and source regions of near-Earth asteroids. Icarus, 222, 273–282.

Harris, A.W., Young, J.W., Scaltriti, F., Zappalà, V., 1984. Lightcurves and phase relations of the Asteroids 82 Alkmene and 444 Gyptis. Icarus 57, 251258.

Jacobson, S.A., Scheeres, D.J., 2011. Long-term Stable Equilibria for Synchronous Binary Asteroids. ApJ Letters, 736, L19.

Kaasalainen, M., Torppa, J., 2001. Optimization Methods for Asteroid Lightcurve Inversion. I. Shape Determination. Icarus, 153, 24.

Kanamaru, M., Sasaki, S., Wieczorek, M., 2019. Density distribution of

asteroid 25143 Itokawa based on smooth terrain shape. Planetary and Space Science, 174, 32-42.

Kitazato, K., Abe, M., Mito, H., Tarusawa, K., Soyano, T., Nishihara, S., Sarugaku, Y., 2004. Photometric behaviour dependent on solar phase angle and physical characteristics of binary near-Earth Asteroid (65803) 1996 GT. Lunar Planet. Sci. 35. Abstract 1623

Marchis, F., Descamps, P., Berthier, J., Hestroffer, D., Vachier, F., Baek, M., Harris, A. W., Nesvorn, D., 2008. Main belt binary asteroidal systems with eccentric mutual orbits. Icarus, 195, 295-316.

McMahon, J., Scheeres, D., 2010a. Secular orbit variation due to solar radiation effects: a detailed model for BYORP. Celest. Mech. Dyn. Astron. 106, 261300.

McMahon, J., Scheeres, D., 2010b. Detailed prediction for the BYORP effect on binary near-Earth Asteroid (66391) 1999 KW4 and implications for the binary population. Icarus, 209, 494–509.

Michel, P., Kueppers, M., Campo Bagatin, A., et al. 2022. PSJ, submitted.

Naidu, S. P. et al. 2020. Radar observations and a physical model of binary near-earth asteroid 65803 Didymos, target of the DART mission, Icarus 348, 113777

Naidu, S. P. et al. 2022. Anticipating the DART impact: Orbit estimation of Dimorphos using a simplified model. Submitted to Planetary Science Journal.

Neish, C. D., Nolan, M. C., Howell, E. S., Rivkin, A. S., 2003. Radar observations of binary asteroid 5381 Sekhmet. In American Astronomical Society Meeting Abstracts, Vol. 203, pp. 134-02.

Ostro, S. J., Margot, J. L., Benner, L. A., Giorgini, J. D., Scheeres, D. J., Fahnestock, E. G., and others, 2006. Radar imaging of binary near-Earth asteroid (66391) 1999 KW4. Science, 314, 1276-1280.

Pravec, P., Benner, L. A. M., Nolan, M. C., et al. 2003, IAUC, 8244.

Pravec, P., et al., 2006, Photometric survey of binary near-Earth asteroids, Icarus, 181:6393.

Pravec, P., Harris, A.W., 2007. Binary asteroid population. 1: Angular momentum content. Icarus 190, 250-259.

Pravec, P., Scheirich, P., 2010. Binary System Candidates for Detection of BYORP. 42nd annual meeting of the Division for Planetary Sciences of the American Astronomical Society, Oct. 3 - Oct. 8, 2010, Pasadena, CA.

Pravec, P., et al. 2012. Absolute magnitudes of asteroids and a revision of asteroid albedo estimates from WISE thermal observations, Icarus 221, 365-387.

Pravec, P., et al. 2022. Photometric observations of the binary near-Earth asteroid

(65803) Didymos in 2015-2021 prior to DART impact. Submitted to Planetary Science Journal.

Rivkin, A. S., Chabot, N. L., Stickle, A. M., et al. 2021, PSJ, 2, 173

Rossi, A., Marzari, F., Farinella, P. 1999. Orbital evolution around irregular bodies. Earth, Planets and Space 51, 1173-1180.

Scheirich, P., and Pravec, P., 2009. Modeling of lightcurves of binary asteroids, Icarus, 200:531547.

Scheirich, P., Pravec, P., Jacobson, S. A., Ďurech, J., Kušnirák, P., Hornoch, K., Mottola, S., Mommert, M., Hellmich, S., Pray, D., Polishook, D., Krugly, Y. N., Inasaridze, R. Y., Kvaratskhelia, O. I., Ayvazian, V., Slyusarev, I., Pittichová, J., Jehin, E., Manfroid, J., Gillon, M., Galád, A., Pollock, J., Licandro, J., Alí-Lagoa, V., Brinsfield, J., Molotov, I. E., 2015. The binary near-Earth Asteroid (175706) 1996 FG_3 – An observational constraint on its orbital evolution. Icarus, 245, 56–63.

Scheirich, P. and 36 colleagues, 2021. A satellite orbit drift in binary near-Earth asteroids (66391) 1999 KW4 and (88710) 2001 SL9 - Indication of the BYORP effect, Icarus 360. doi:10.1016/j.icarus.2021.114321

Vokrouhlický, D., Čapek, D., Chesley, S. R., Ostro, S. J., 2005. Yarkovsky detection opportunities. II. Binary systems. Icarus, 179, 128–138

Yeomans, D. K., Antreasian, P. G., Barriot, J. P., Chesley, S. R., Dunham, D. W., Farquhar, R. W., and 10 others, 2000. Radio science results during the NEAR-Shoemaker spacecraft rendezvous with Eros. Science, 289, 2085-2088.

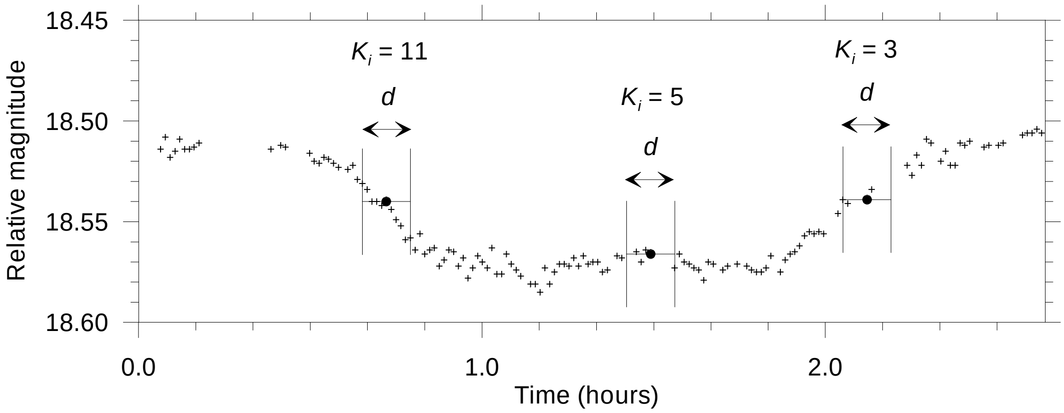

Fig. 1. An example of the determination of the weights applied to individual data points, as described in Section 2.2. The observed data are marked as crosses. For each data point, the number K_i of all data points that are within $\pm d/2$ from the given point is calculated (for the three examples shown, $K_i = 11$, 5 and 3). d is the correlation time, which we set equal to 0.14 h. A contribution of each data point to the χ^2 sum is then weighted by $1/K_i$.

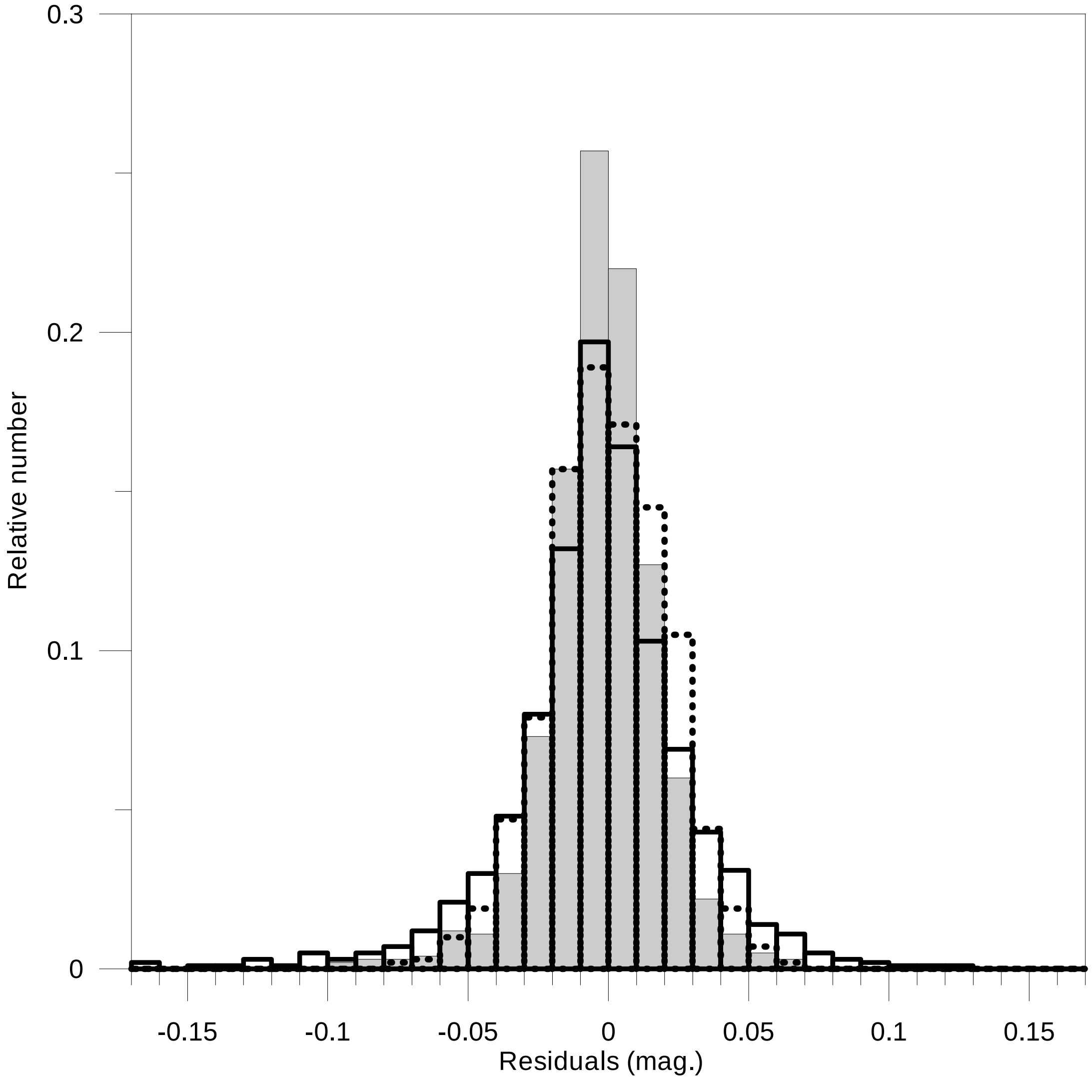

Fig. 2. Distribution of residuals of the model fitted to the observational data without the application of weights described in Section 2.2 (grey area) and with the weights applied (thick solid line). A histogram of a set of randomly generated values with normal distribution and standard deviation of 0.0216 mag. (thick dotted line) is shown for comparison.

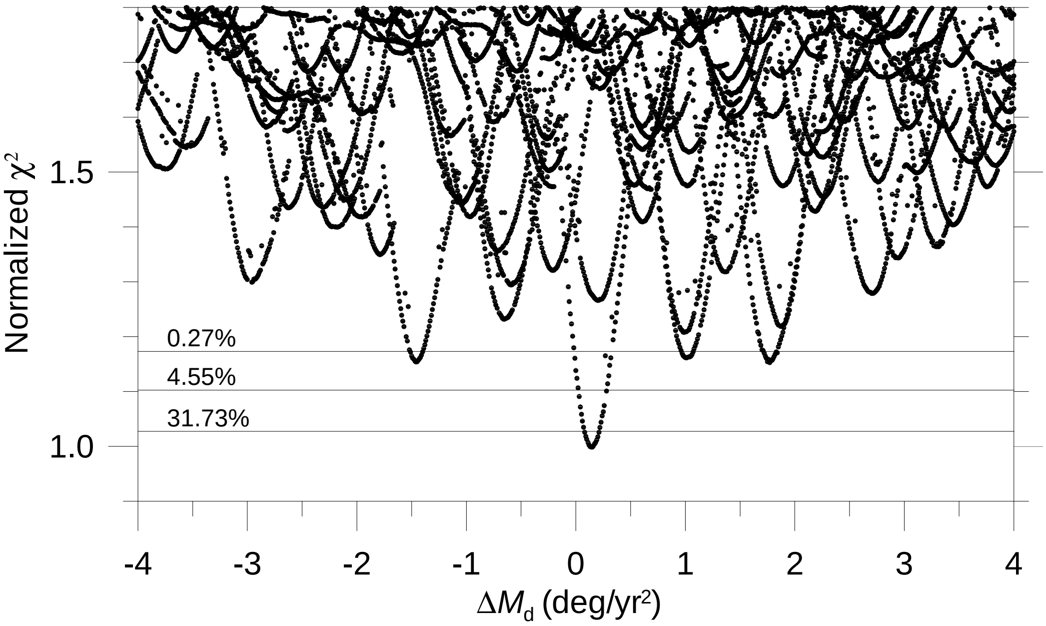

Fig. 3. The normalized χ^2 vs. ΔM_d for solutions of the model presented in Section 2.2. The three horizontal lines give the p-values – the probabilities that the χ^2 exceeds a particular value only by chance, corresponding to 1-, 2- and 3σ interval of the χ^2 distribution with 567 degrees of freedom. See text for details.

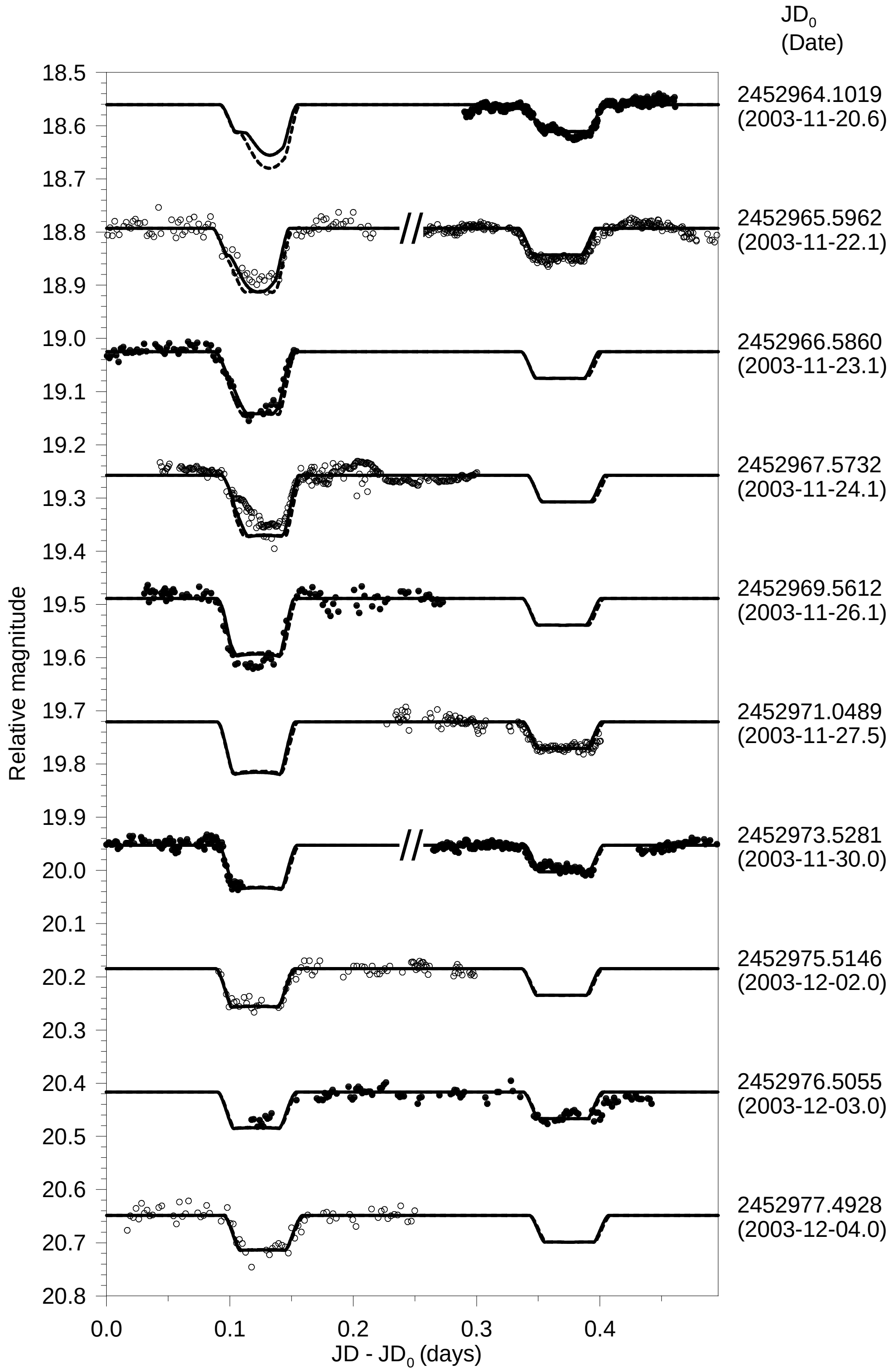

Fig. 4. The orbital lightcurve component of the Didymos system. The observed data are marked as points. (To avoid confusion between different data sets, solid and empty symbols are used alternating on each plot.) The solid curve represents the synthetic lightcurve for the best-fit solution. For comparison, the dashed curve is the model with ΔM_d fixed at 0.0 deg/yr^2 and all other parameters varied to obtain the best fit. The primary and secondary events (the terms refer to which of the two bodies is occulted or eclipsed) are always shown on the left and right side of the plots, respectively. In some cases, the observations of a secondary event precede that of a primary event (i.e., their order in the dataset is inverse of that shown on the plot). In order to save space in the plot, we present these events in reverse order to how they were observed. They are separated by "//" symbol in the plot and one orbital period (0.496 d) is to be subtracted from x coordinate of data points to the right from this separator.

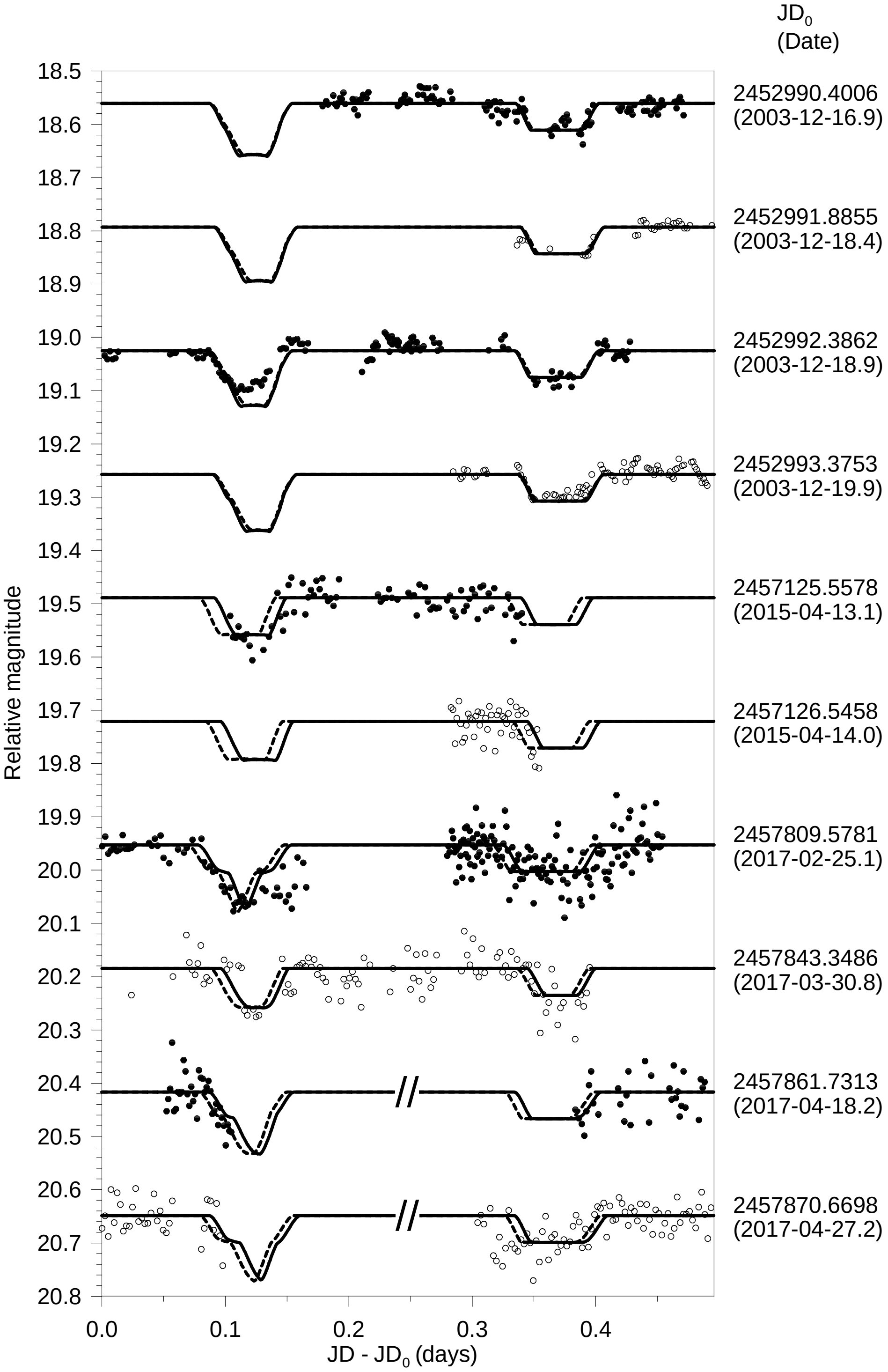

Fig. 5. Continuation of Fig. 4.

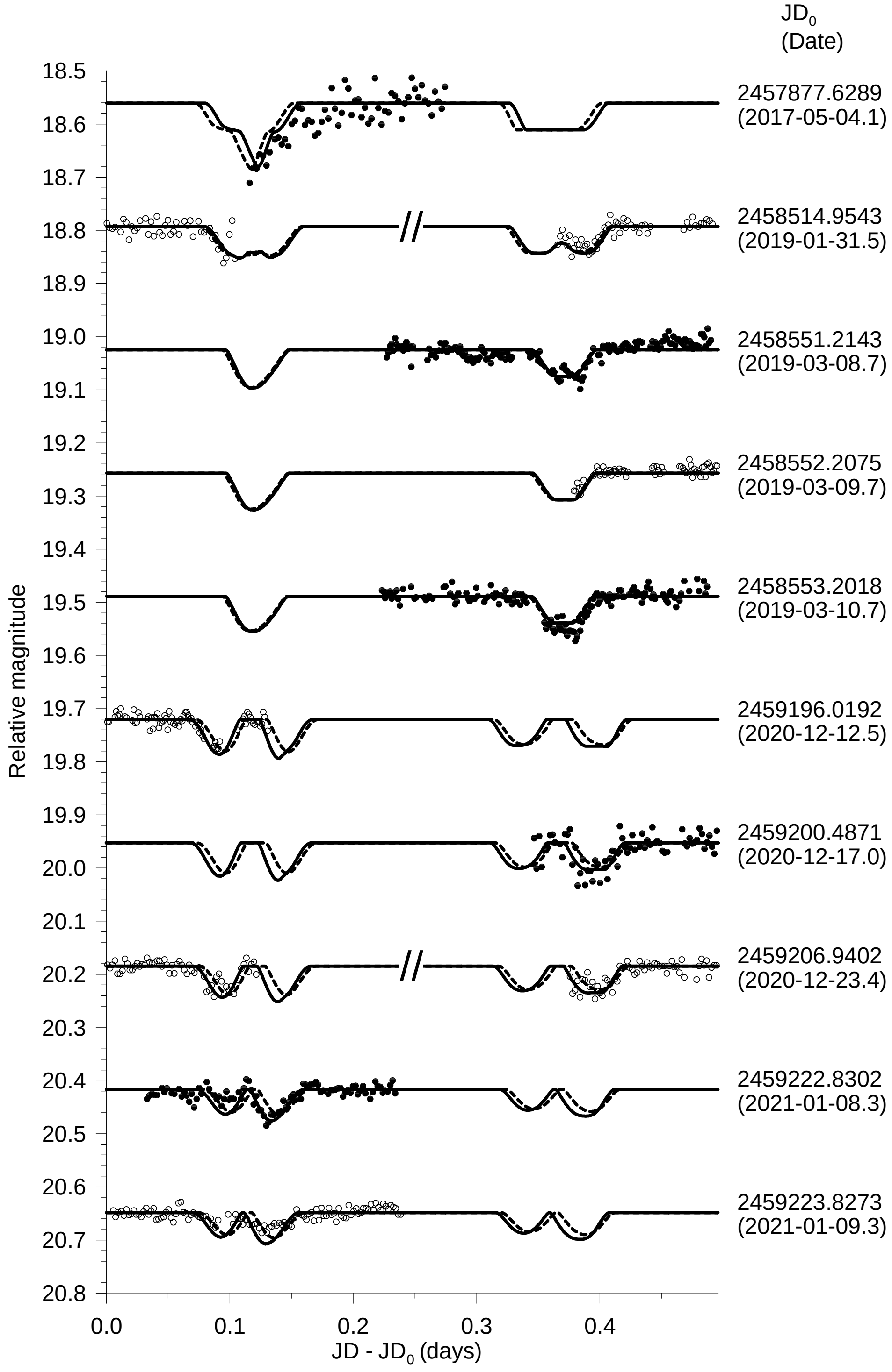

Fig. 6. Continuation of Fig. 4.

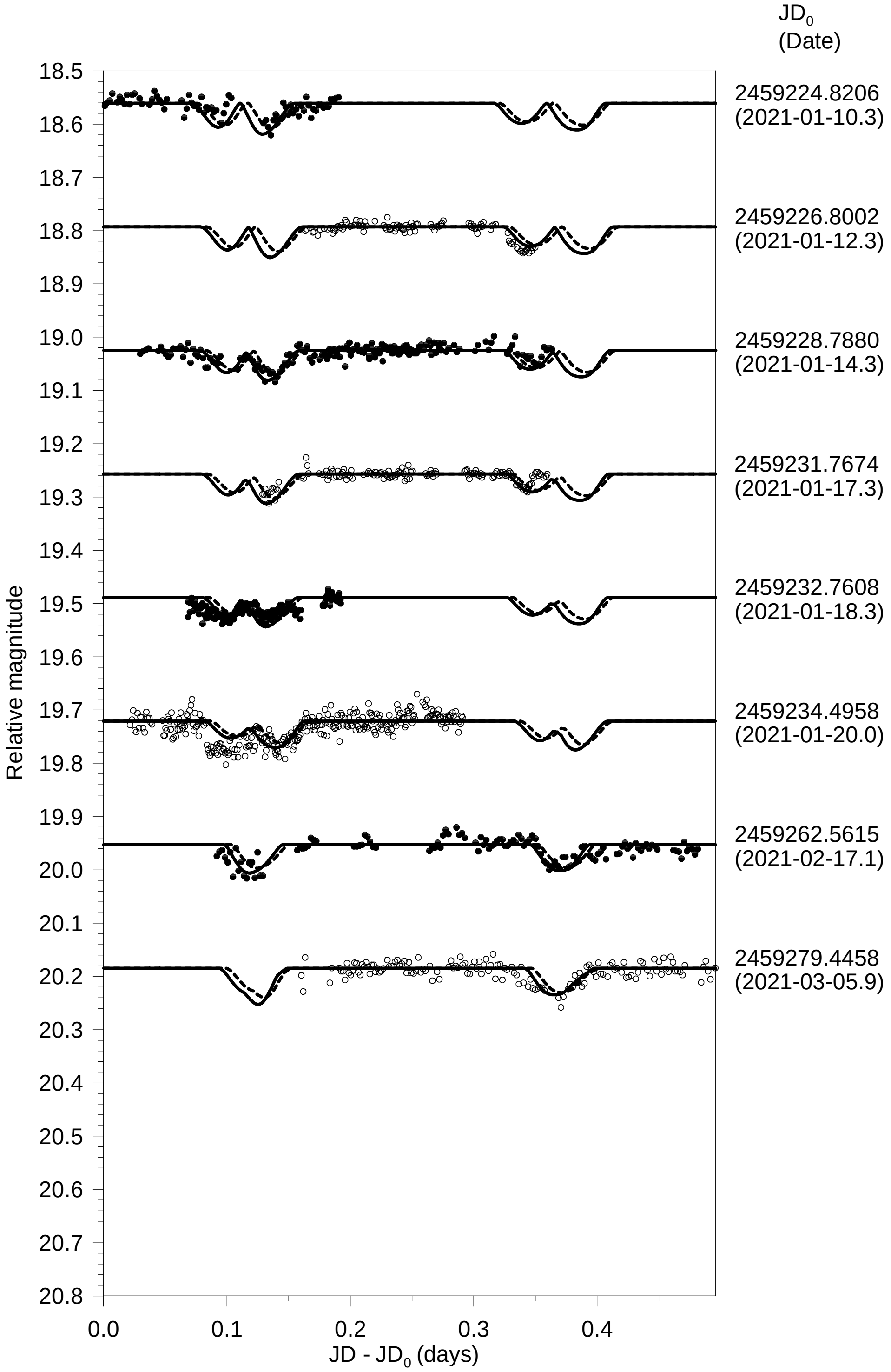

Fig. 7. Continuation of Fig. 4.

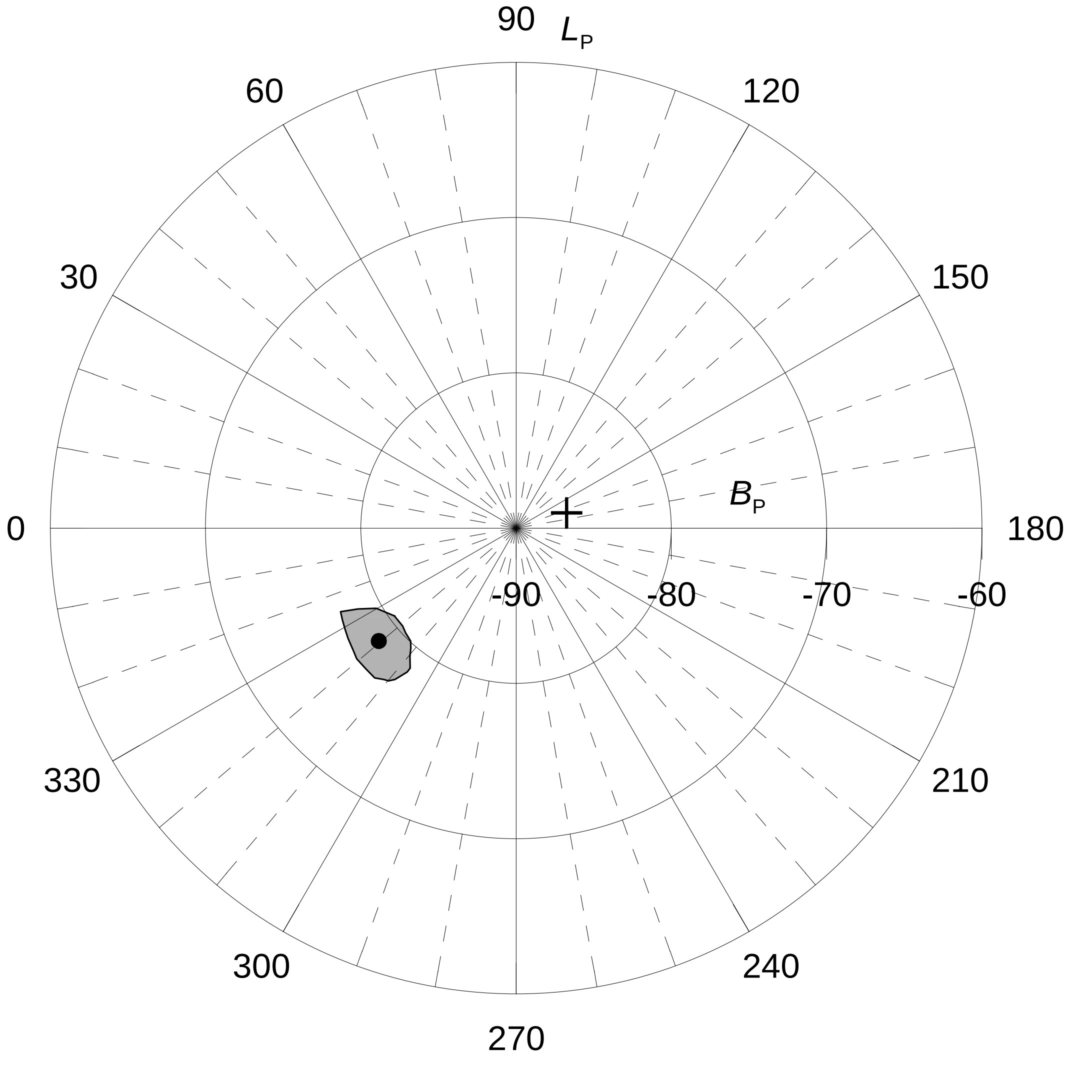

Fig. 8. Area of admissible poles for the mutual orbit of Didymos in ecliptic coordinates (grey area). The dot is the nominal solution given in Table 2. This area corresponds to 3σ confidence level. The south pole of the current asteroid's heliocentric orbit is marked with the cross.

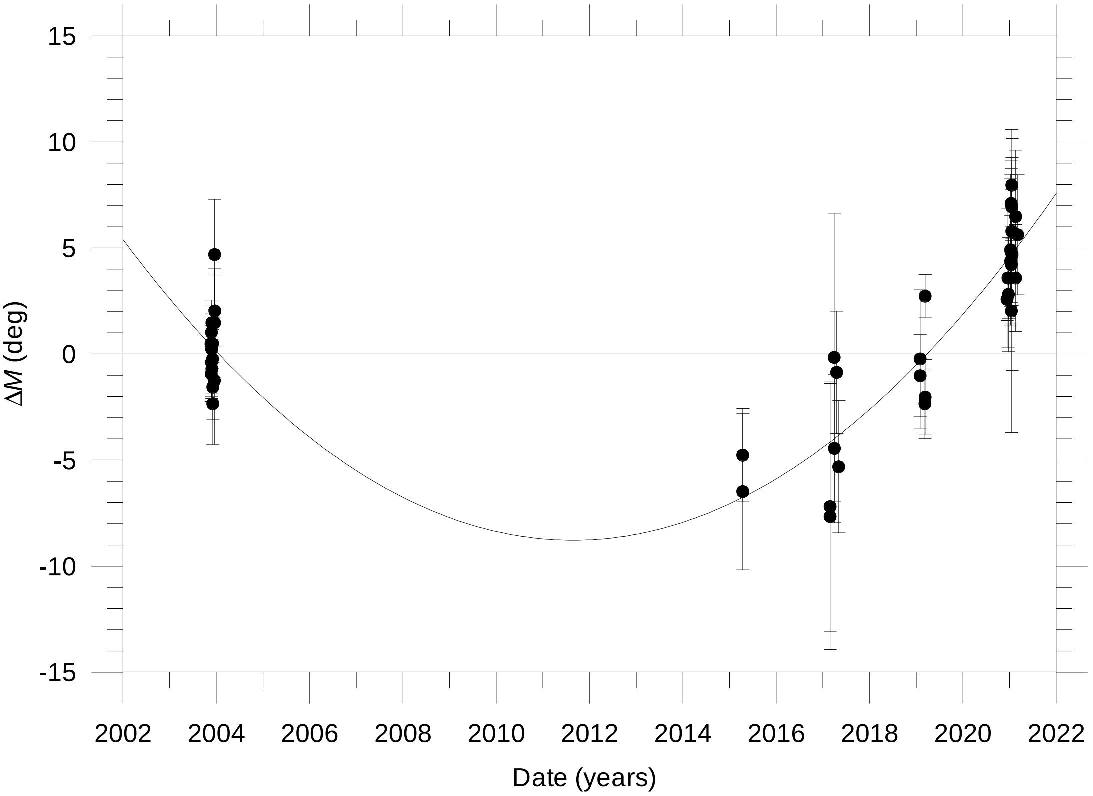

Fig. 9. Time evolution of the mean anomaly difference ΔM with respect to the solution with $\Delta M_d = 0$. See text for details. Each point corresponds to a mutual event covered by the observed data. Vertical error bars represent estimated 1σ uncertainties of the event times, expressed in the mean anomaly. A quadratic fit to the data points, represented by the solid curve, gives the quadratic term of 0.152 deg/yr^2.

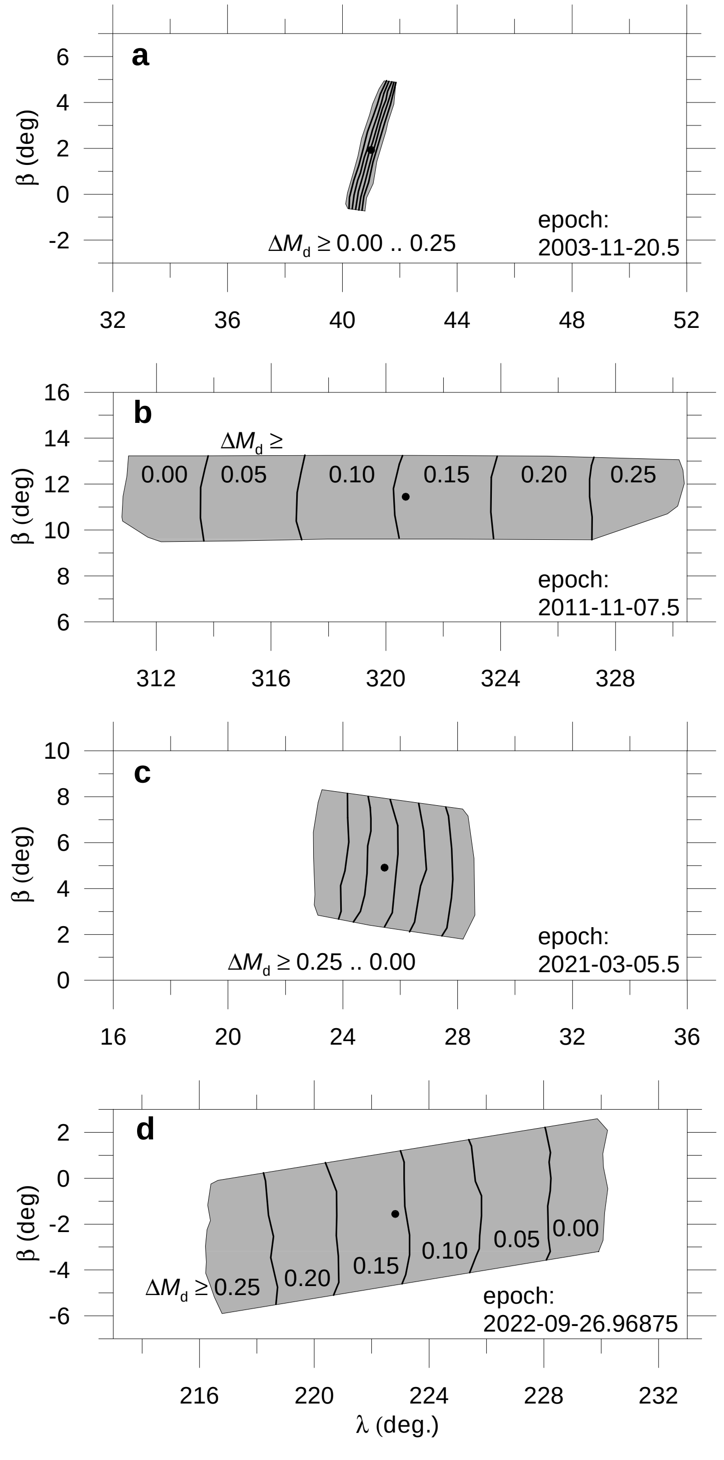

Fig. 10. 3-σ uncertainty area of Dimorphos relative position with respect to Didymos expressed in ecliptical coordinates λ, β (grey areas). To demonstrate the change in size of the uncertainty area with time, we plotted the area for four epochs (2003-11-20.5 – the beginning of the first apparition in 2003; 2011-11-07.5 – epoch JD0; 2021-03-05.5 – the end of the last apparition in 2021; 2022-09-26.96875 – the nominal epoch of the DART impact; panels a, b, c, d, respectively) with the same scale of the axes on all four panels. To show a correlation between λ and ΔM_d, the approximately vertical lines divide areas with $\Delta M_d \geq 0.00; 0.05; 0.10; 0.15; 0.20; 0.25$ deg/yr^2, respectively (the inequality is used becease ΔM_d is correlated with other parameters as well and therefore strict boundaries for its values cannot be given). The dots denote the nominal solution given in Table 2.

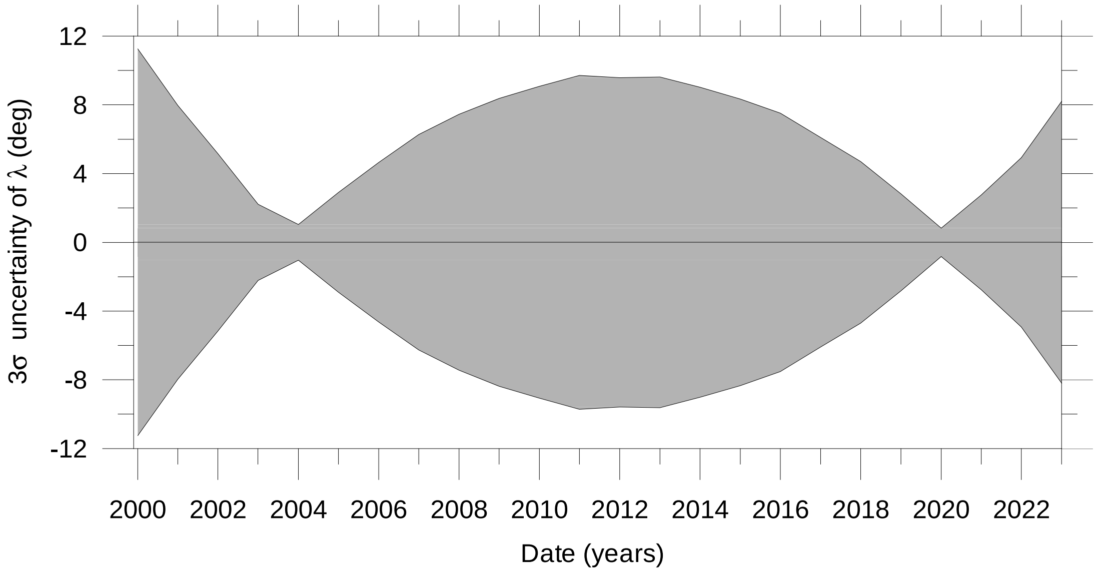

Fig. 11. Evolution of the 3-σ uncertainty of the ecliptic longitude (λ) of the radius vector of Dimorphos with respect to Didymos in time.